Scalar decay in a three-dimensional chaotic flow

K. Ngan*

Met Office, Exeter EX1 3PB, UK

J. Vanneste†

School of Mathematics and Maxwell Institute for Mathematical Sciences, University of Edinburgh, Edinburgh EH9 3JZ, UK

(Dated: March 2011)

Abstract

The decay of a passive scalar in a three-dimensional chaotic flow is studied using high-resolution numerical simulations. The (volume-preserving) flow considered is a three-dimensional extension of the randomised alternating sine flow employed extensively in studies of mixing in two dimensions. It is used to show that theoretical predictions for two-dimensional flows with small diffusivity carry over to three dimensions even though the stretching properties differ significantly. The variance decay rate, scalar field structure, and time evolution of statistical moments confirm that there are two distinct regimes of scalar decay: a locally controlled regime, which applies when the domain size is comparable to the characteristic lengthscale of the velocity field, and a globally controlled regime, which when applies when the domain is larger. Asymptotic predictions for the variance decay rate in both regimes show excellent agreement with the numerical results. Consideration of both the forward flow and its time reverse makes it possible to compare the scalar evolution in flows with one or two expanding directions; simulations confirm the theoretical prediction that the decay rate of the scalar is the same in both flows, despite the very different scalar field structures.

PACS numbers: 47.51.+a,05.45.-a,47.52.+j,05.10.-a

*keith.ngan@metoffice.gov.uk

†J.Vanneste@ed.ac.uk

I. INTRODUCTION

In studies of fluid mixing, much attention has been devoted to chaotic-advection flows, characterised by relatively simple (smooth and divergence-free) velocity fields but complex, chaotic particle trajectories. Flows of this type appear in several contexts: Stokes flows [1], turbulent flows with large Schmidt number (in the so-called Batchelor regime [2]), geophysical flows [3, 4], and elastic turbulence [5]. One aspect is of particular interest: the decay, through the combined effect of advection and diffusion, of the concentration of passive scalars released in such flows. In bounded domains this decay is exponentially fast; one of the main problems is then to relate the corresponding decay rate to the flow characteristics and to the diffusivity.

For small diffusivity $\kappa \to 0$, a clear distinction emerges between flows that are everywhere chaotic (e.g. uniformly hyperbolic), and flows with regular regions (e.g. containing elliptic islands [6] or incorporating no-slip boundary conditions [7, 8]): the decay rate of passive scalars tends to a non-zero limit as $\kappa \to 0$ in the first case, whereas it tends to zero in the second case. In this paper, we concentrate on the first case and, more specifically, on stochastic models of chaotic flows. These models, in which the complex time dependence of realistic flows is represented by random processes [9, 10], have been the subject of sustained research from the mid 1990s onward [11]. Remarkably, several theoretical results are now available which relate properties of the scalar decay, notably the decay rate, to flow properties such as stretching statistics [12–19]. These results, which we review in Sec. II below, have been confirmed by numerical simulations [18, 19]. Confirmation, however, has been limited to two-dimensional flows. The main aim of the present paper is to test the theoretical results against numerical simulations of three-dimensional flows.

The passage from two to three dimensions adds significantly complexity to the problem. Numerically, the high resolutions needed to capture the fine scalar scales generated for small diffusivities make the 3D case much more computationally demanding than 2D. Physically, the dynamics of scalars in 3D flows are also much richer than in 2D flows: incompressibility provides a strong constraint in 2D, leading in particular to equal and opposite (stretching) Lyapunov exponents; in 3D incompressibility represents a looser constraint, imposing only that the sum of the three Lyapunov exponents vanish. The existence of three distinct Lyapunov exponents also has a profound influence on the concentration field. Depending

on whether the intermediate Lyapunov exponent is positive or negative, the concentration field is dominated either by quasi-two-dimensional structures ("pancakes") or by quasi-one-dimensional structures ("needles"). Interestingly, the most recent theoretical results about the scalar decay rate [18, 19] are insensitive to this difference in structure and make predictions that are independent of the sign of the intermediate Lyapunov exponent. Our simulations confirm the validity of this conclusion.

A well-known difference between mixing in 2D and 3D is that chaotic particle trajectories are only possible in 2D flows if they are time dependent, whereas they exist in time-independent 3D flows. Time-independent 3D flows, however, are similar to one-degree-of-freedom Hamiltonian maps [20], and do not lead to global chaos but rather to a mixture of chaotic and (possibly small) regular regions, with the latter controlling scalar decay in the long-time limit. The flows with random time dependence that we consider do not have this type of intricate structure: they are statistically homogeneous and globally mixing. This is one of the aspects which differentiate this paper form earlier work on mixing in 3D, in particular the numerical simulations of time-independent flows in [21] and [22].

Qualitatively, the mixing properties of sufficiently chaotic flows are independent of the flow details. It is therefore advantageous to devise a random-flow model that is easy to implement and analyse. In 2D, this role is played by the randomised sine map [23, 24] which has been used extensively in studies of passive and reactive scalars. In this paper, we propose a straightforward 3D extension of the sine map. With the parameters chosen, this map has two positive and one negative Lyapunov exponent, which yield concentration fields with pancake-like structure. We use the associated inverse map as a model for flows with two negative and one positive Lyapunov exponent which generate needle-like concentration fields. The extension to 3D is not uniquely defined. Other versions of the 3D map are less mixing in that they do not stretch certain fixed directions. We briefly comment on the impact this property has on the scalar decay.

The plan of the paper is as follows. In Sec. II, we review the theoretical predictions for the decay rate of the scalar concentration. Following [19], we emphasise the existence of two regimes of scalar decay: a locally controlled regime relevant to flows whose typical scale is comparable to the size of the (periodic) domain considered, and a globally controlled regime relevant to flows of smaller scale (see also [18]). The three-dimensional sine map is introduced in Sec. III. There we examine the stretching properties of the map and describe

the numerical procedure employed for simulations of the scalar evolution. Secs. IV and V present results of simulations carried out in different domain sizes. This makes it possible to explore both locally and globally controlled regimes and contrast differences in the decay rate as well as in the structure of the concentration field. We also compare concentration fields obtained with the map and its inverse. The paper concludes with a discussion in Sec. VI.

II. DECAY RATE

The evolution of the concentration $C(\boldsymbol{x}, t)$ of a passive scalar released in a flow $\boldsymbol{v}(\boldsymbol{x}, t)$ is governed by the advection–diffusion equation

$$\partial_t C + \boldsymbol{v} \cdot \nabla C = \kappa \nabla^2 C, \tag{1}$$

with initial conditions $C(\boldsymbol{x}, 0) = C_0(\boldsymbol{x})$. When non-dimensionalised using characteristic length and velocity scales, this problem retains its form, with κ now representing the inverse Péclet number rather than the diffusivity. This non-dimensional interpretation will be used in what follows.

We focus on incompressible flows, $\nabla \cdot \boldsymbol{v} = 0$, generated by specific random processes. These flows are assumed to have homogeneous and stationary statistics and to be spatially smooth, that is, $\|\boldsymbol{v}(\boldsymbol{x}) - \boldsymbol{v}(\boldsymbol{x}')\| \propto \|\boldsymbol{x} - \boldsymbol{x}'\|$ as $\|\boldsymbol{x} - \boldsymbol{x}'\| \to 0$. Periodic boundary conditions are applied to (1). Since (1) is left unchanged when a constant is added to C, there is no loss of generality in assuming that the concentration field averages to zero:

$$\int C(\boldsymbol{x}, t)\, \mathrm{d}\boldsymbol{x} = \int C_0(\mathbf{x})\, \mathrm{d}\boldsymbol{x} = 0. \tag{2}$$

By analogy with the finite-dimensional case the concentration $C(\boldsymbol{x}, t)$ can be expected to decay exponentially in the long-time limit:

$$C(\boldsymbol{x}, t) \sim D(\boldsymbol{x}, t)\mathrm{e}^{-\lambda t} \quad \text{as} \quad \to \infty \tag{3}$$

for almost all realisations of $\boldsymbol{v}(\boldsymbol{x}, t)$, Here the deterministic decay rate λ is best interpreted as (minus) the Lyapunov exponent of the linear system (1), and $D(\boldsymbol{x}, t)$ is a stationary function termed strange eigenmode [23] (see [25] for rigorous results). We emphasise that λ is the Lyapunov exponent of the infinite-dimensional random system (1) and should not be

confused with the Lyapunov exponent of the three-dimensional linear system governing the separation of nearby particles in the velocity field $\boldsymbol{v}$. We also note that λ^{-1} is not the only useful time scale characterising the scalar decay: a dissipation time scale can for instance be defined as the time for some norm of C to be reduced from its initial value by a given fraction [26]; this, however, characterises the early-time behaviour rather than the long-time behaviour on which we focus.

A striking feature of the decay rate is that it tends to a non-zero value in the limit of zero diffusivity (infinite Péclet number), $\lim_{\kappa\to 0}\lambda = \lambda_0 \neq 0$, provided the flow is sufficiently mixing. This raises the question of the relationship between the asymptotic decay rate, λ_0, and the statistical properties of the flow, $\boldsymbol{v}(\boldsymbol{x}, t)$.

In a series of papers [11–14], λ_0 has been related to the large-deviation statistics of the finite-time Lyapunov exponents of $\boldsymbol{v}(\boldsymbol{x}, t)$. These are defined as

$$h = t^{-1}\log\|\boldsymbol{y}\|, \tag{4}$$

where $\boldsymbol{y}$ denotes the separation between nearby trajectories, and are distributed according to a pdf, $p(h;t)$ say. λ_0 may be expressed in terms of the rate function

$$g(h) = -\lim_{t\to\infty}\log p(h;t) \tag{5}$$

associated with this pdf. Alternatively, it may be expressed in terms of the generalised Lyapunov exponent

$$\ell(q) = \lim_{t\to\infty} t^{-1}\log \mathsf{E}\,\|\boldsymbol{y}\|^q, \tag{6}$$

where E denotes ensemble average. These formulations are equivalent since $g(q)$ and $\ell(q)$ are related by a Legendre transform [27, 28]:

$$\ell(q) = \sup_h\left(qh - g(h)\right). \tag{7}$$

Results of this type are not general, however. In particular, they do not apply to flows whose typical scale is much smaller than the domain size [15, 16, 29, 30]. In fact there are two different regimes of scalar decay [17–19]. Flows whose spatial scale is comparable to the domain size are in a *locally controlled* regime, in which λ_0 depends only on the stretching statistics of $\boldsymbol{v}(\boldsymbol{x}, t)$ and is given in terms of $g(h)$ or $\ell(q)$. Flows with smaller scale, on the other hand, are in a *globally controlled* regime, in which λ_0 depends on global flow features including the domain size.

In [19], the two regimes are related to two different parts of the spectrum of the (deterministic) linear operator governing the evolution of the covariance $\mathsf{E}\,C(\boldsymbol{x},t)C(\boldsymbol{x}',t)$ in Kraichan–Kazantsev and renewing flows [31]. The smallest non-zero eigenvalue determines $\bar{\gamma}$, the decay rate of the ensemble-averaged variance:

$$\bar{\gamma} = -\lim_{t\to\infty} t^{-1} \log \mathsf{E} \int C^2(\boldsymbol{x},t)\,\mathrm{d}\boldsymbol{x}. \tag{8}$$

In the locally controlled regime, $\bar{\gamma}$ belongs to the continuous spectrum of the operator obtained for $\kappa = 0$, while in the globally controlled regime, $\bar{\gamma}$ represents a discrete eigenvalue.

Because of this difference in the eigenvalues, the decay rates are qualitatively different in the two regimes. In the locally controlled regime the asymptotic form of $\bar{\gamma}$ for $\kappa \to 0$ is

$$\bar{\gamma}_{\mathrm{local}} = -\ell(q_*) + \frac{2\pi^2 \ell''(q_*)}{\log^2 \kappa} + o(1/\log^2 \kappa), \tag{9}$$

where q_* is the minimum of $\ell(q)$ [so that $\ell(q_*) = -g(0)$, see (7)]. In the globally controlled regime, no such simple expression exists, and the leading-order term can be obtained only by solving the eigenvalue problem for the covariance. However, in the limit of flow scale much smaller than domain size, a useful estimate is provided by homogenisation theory, which approximates (1) by a diffusion equation with an effective diffusivity κ_{eff} [32], whence

$$\bar{\gamma}_{\mathrm{global}} \sim \bar{\gamma}_{\mathrm{hom}} = \frac{8\pi^2 \kappa_{\mathrm{eff}}}{L^2}, \tag{10}$$

where L is the largest of the domain periods.

Note that (9) and (10) describe the decay rate of the ensemble-averaged variance. The decay rate of a single realisation is given by

$$\gamma = -\lim_{t\to\infty} t^{-1} \log \int C^2(\boldsymbol{x},t)\,\mathrm{d}\boldsymbol{x} = 2\lambda \tag{11}$$

on using (3). In general, $\gamma \neq \bar{\gamma}$, the difference marking the intermittency of the scalar decay [33]. For the flows considered here, differences between γ and $\bar{\gamma}$ are negligible (see Sec. IV). Indeed we will confirm that (9) can be used to predict the variance decay in single realisations. (The equality of γ and $\bar{\gamma}$ in the homogenisation limit (10) is clear since the spatially homogenised equation is deterministic.)

The theory summarised above holds in any dimension [19]. Until now, numerical verification (of (9) and (10) in particular) has been restricted to two dimensions. In this paper we assess the applicability to three-dimensional flows.

The additional dimension introduces interesting complexities. In two dimensions, incompressibility strongly constrains the distribution of finite-time Lyapunov exponents, leading to the symmetry property $\ell(q) = \ell(-q-2)$. As a result, $q_* = -1$ and the leading-order of (9), which in general reads $\bar{\gamma} \sim -\ell(q_*) = g(0)$, can be alternatively computed as $\bar{\gamma} \sim -\ell(-1)$ (it is in this form that the decay rate appears in some of the theories [12, 13, 18]). In dimensions $d \geq 2$, by contrast, there is no such symmetry property; rather what hold are the relationships [28]

$$\ell^-(q) = \ell(-q-d), \quad \text{and hence} \quad g^-(h) = g(-h) - dh \tag{12}$$

between the stretching statistics of a flow and those of the time-reversed flow (denoted by $^-$). A consequence is that (9) predicts that the decay rate of a scalar is the same in a flow and in the time-reversed flow. This is a remarkable prediction for $d = 3$ because many features of the stretching in a flow and its time-reverse are different. In particular, the intermediate Lyapunov exponent changes sign; thus, if a flow has one contracting and two expanding directions, the time-reverse has one expanding and two contracting directions. As a result, the scalar fields have very different structures in the two flows, with typical concentration isosurfaces taking the shape of (nearly two-dimensional) pancakes in one case and the shape of (nearly one-dimensional) needles in the other. Nonetheless, the scalar concentration decays at the same rate, as we verify below [34].

III. THREE-DIMENSIONAL SINE MAP

A. Formulation

The randomised two-dimensional sine map [23, 24] has become a standard tool for the study of mixing by spatially smooth flows. It is given by

$$x_{n+1} = x_n + a\sin(y_n + \phi_n), \quad y_{n+1} = y_n + b\sin(x_{n+1} + \psi_n), \tag{13}$$

where a and b are constant parameters and ϕ_n and ψ_n are independent random angles uniformly distributed in $[0, 2\pi]$. The domain considered is periodic so the right-hand sides in (13) are taken modulo 2π. This map provides the positions at times $n\tau$, $n = 1, 2\cdots$ of particles advected by a succession of shear flows alternating in direction. Its application to (1) is straightforward: advection of a scalar field by (13) can be implemented very efficiently

using a lattice representation; diffusion for small κ can be incorporated as smoothing by the heat kernel $\propto \exp(-(x^2+y^2)/(4\kappa\tau))$ (or rather the periodised version thereof).

In what follows, we use a straightforward three-dimensional generalisation of (13), namely

$$x_{n+1} = x_n + a\sin(y_n+\phi_n), \quad y_{n+1} = y_n + b\sin(z_n+\psi_n), \quad z_{n+1} = z_n + c\sin(x_{n+1}+\varphi_n), \tag{14}$$

where a, b and c are constant, and ϕ_n, ψ_n and φ_n are independent uniformly distributed random phases in $[0, 2\pi]$. This map, which corresponds to successive applications of shear flows in the x-, y- and z-directions, preserves volume and has homogeneous statistics. As in two dimensions, these shear flows are simple enough that they can be integrated explicitly to yield (14). The stretching statistics of the map are controlled by the Jacobian matrix, given at the origin by

$$A_n = \begin{pmatrix} 1 & a\cos\phi_n & 0 \\ 0 & 1 & b\cos\psi_n \\ c\cos(a\sin\phi_n+\varphi_n) & ac\cos\phi_n\cos(a\sin\phi_n+\varphi_n) & 1 \end{pmatrix}. \tag{15}$$

The three Lyapunov exponents are computed numerically from the singular values of $A_nA_{n-1}\cdots A_0$. In what follows, we fix $a = b = c = \pi$. In this case, the Lyapunov exponents are found to be 1.04, 0.58 and -1.62. Thus the map (14) has one contracting and two expanding directions.

The inverse map,

$$z_{n+1} = z_n + c\sin(x_n+\varphi_n), \quad y_{n+1} = y_n + b\sin(z_{n+1}+\psi_n), \quad x_{n+1} = x_n + a\sin(y_{n+1}+\phi_n), \tag{16}$$

corresponds to the time-reversed flow. It has Jacobian matrix A_n^{-1}, and for $a = b = c = \pi$ Lyapunov exponents 1.62, -0.58 and -1.04, hence one expanding and two contracting directions.

Three-dimensional generalisations of (13) are not uniquely determined. Maps differing from (14) and (16) via permutations of the variables can be constructed. However, they may not be transitive, in the sense that their Jacobian matrices have invariant directions independent of the random phases. Such maps may not be sufficiently mixing for predictions such as (9) to hold, even if the largest Lyapunov exponent is positive. We return to this point in Sec. VI.

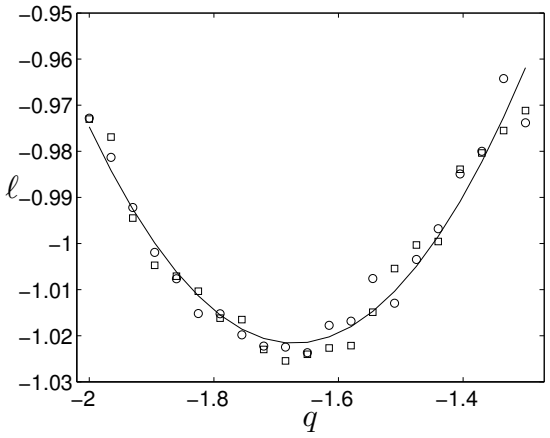

FIG. 1. Generalised Lyapunov exponents for the map (14) with $a = b = c = \pi$. The results of two Monte Carlo computations (circles and squares) are shown together with the best fit by a parabola.

B. Theoretical predictions

We now consider the predictions (9)–(10) for the three-dimensional map (14) and its inverse (16). We choose the parameters $a = b = c = \pi$ and take $\tau = 1$.

In order to find the coefficients in the asymptotic formula (9), we use a Monte Carlo approach to compute $\ell(q)$ numerically in the vicinity of its minimum, q_*. Because the expectation, $\mathsf{E}\,\|\boldsymbol{y}\|^q$, is dominated by rare realisations, the sampling required is rather delicate; we therefore use importance sampling, namely the random resampling method described in [28]. In particular, we use an ensemble of 5×10^4 realisations to estimate $\ell(q)$ over a range bracketing q_*, $q \in [-2, -1.4]$; $\ell(q_*)$ and $\ell''(q_*)$ follow from a parabolic fit. Some numerical results are shown in Figure 1. Rough error bars are obtained by repeating this procedure 10 times. This provides the estimates $\ell(q_*) = 1.022 \pm 0.002$ and $\ell''(q_*) = 0.93 \pm 0.09$. Introducing these values into (9) then yields the estimate

$$\bar{\gamma}_{\rm local} = 1.022(\pm 0.002) + \frac{18.36(\pm 1.78)}{\log^2 \kappa}. \tag{17}$$

for the variance decay rate in the locally controlled regime. This is tested in Sec. IV.

The corresponding prediction for the inverse map (16) is exactly the same as that for the direct map (14). Indeed, Eq. (12) implies that $\ell^-(q)$ is the reflection of $\ell(q)$ about the line $q = -3/2$. Therefore, $\ell^-(q_*) = \ell(q_*)$, $(\ell^-)''(q_*) = \ell''(q_*)$ and hence $\gamma_{\rm local}$ is unchanged.

To examine both locally and globally controlled regimes of scalar decay, we consider

the scalar evolution for the forward map in a periodic cube of (total) length $2\pi P$ with $P = 1, 2 \cdots$; that is, the flow has unit cells of length 2π but the right-hand sides of (14) are taken modulo $2\pi P$. The asymptotic result (9) is expected to hold for small values of P, while the homogenisation approximation (10) should be valid for $P \gg 1$. The effective diffusivity κ_{eff} appearing in (10), is easily found by recalling that the variance of one of the coordinates, x_n say, satisfies $\mathsf{E}\, x_n^2 = 2\kappa_{\text{eff}} n$; computing the variance from (14) gives $\kappa_{\text{eff}} = a^2/4$. Hence

$$\bar{\gamma}_{\text{global}} \sim \bar{\gamma}_{\text{hom}} = \frac{\pi^2}{2P^2}. \tag{18}$$

for large P.

We wish to estimate the value of P at which the transition from local to global control occurs. The predicted decay rate $\bar{\gamma}$ is determined by whichever of the local and global decay rates is smaller. Comparing (17) with (18) we therefore expect local control for $P = 1, 2$ and global control for $P \geq 3$.

C. Numerical procedure

Numerical simulations are performed on a regular grid of N^3 points. The advection uses the 3-D sine map (14), while for numerical efficiency the diffusion is applied in spectral space using a Fast Fourier Transform. We have confirmed that an explicit finite-difference step yields essentially indistinguishable results. The code has been tested by reproducing results of [19] for the 2-D sine map (13).

Two sets of initial conditions are considered. In most simulations we use

$$C(\boldsymbol{x}, 0) = \sin(x/P)\sin(y/P)\sin(z/P). \tag{19}$$

In Sec. V, we also use the initial condition

$$C(\boldsymbol{x}, 0) = \sin(z/P) \tag{20}$$

corresponding to one of the gravest modes of the diffusion operator in the domain.

The simulations need to resolve spatial scales in the range between the box size, L_0, and the tracer microscale, L_κ. The latter scale is estimated by matching the diffusive and stretching timescales, yielding $L_\kappa = \sqrt{\kappa/\lambda}$, where λ is the largest Lyapunov exponent of $\boldsymbol{v}$. Thus we require $L_\kappa \gtrsim \Delta x$, where $\Delta x = L_0/N$ is the grid spacing, or

$$\kappa \gtrsim (\frac{2\pi}{N})^2 \lambda. \tag{21}$$

In the simulations of Secs. IV and V, $N = 1024$. This implies a critical value of the diffusivity, $\kappa_c = O(10^{-5})$.

For $P > 1$, the numerical simulations are performed on the N^3 grid but with P^3 replicas of the velocity field. Taking $P > 1$ amounts to a redefinition of L_0. For simplicity, however, it is convenient to keep $L_0 = 2\pi$ fixed and rescale the equations. This allows us to reuse the code described above with minimal changes. More precisely, we use the modified map

$$x_{n+1} = x_n + \frac{a}{P}\sin(Py_n + \phi_n), \quad y_{n+1} = y_n + \frac{b}{P}\sin(Pz_n + \psi_n),$$
$$z_{n+1} = z_n + \frac{c}{P}\sin(Px_{n+1} + \varphi_n), \tag{22}$$

with the scaling $\kappa \mapsto P^2\kappa$ and the right-hand sides taken modulo 2π. Note that the Jacobian is unchanged.

IV. LOCAL CONTROL: $P = 1$

In this section, we focus on the locally controlled regime and take $P = 1$. We report on simulations of the forward map (14) for several values of κ in the range 10^{-5}–10^{-1}, and of the inverse map (16) for $\kappa = 10^{-4}$.

The evolution of the variance

$$\sigma^2(n) = \int C^2(\boldsymbol{x}, n)\,\mathrm{d}\boldsymbol{x} \tag{23}$$

in these simulations is shown in Fig. 2(a). As with the two-dimensional sine map (13), the variance decays exponentially after a brief initial transient, in agreement with the strange-eigenmode prediction (3). These results are insensitive to resolution: simulations at the lower resolution $N = 512$ (not shown) are almost identical. Also, there is little variability between different realisations. For an ensemble of 8 realisations evaluated at $N = 512$ (not shown), the decay rate of the variance for $\kappa = 10^{-4}$ varies by about 2%. This difference is of the same order of magnitude as the difference between the decay rates for $N = 512$ and $N = 1024$. We therefore conclude that the intermittency is negligible and henceforth restrict attention to the single-realisation decay rate γ which we identify with $\bar{\gamma}$.

The forward and inverse maps lead to almost identical decay rates. Specifically, for $\kappa = 10^{-4}$, the decay rates for the forward and inverse maps are 1.22 and 1.21, respectively. This supports the claim made in Sec. III B that their decay rates are equal despite differences in their stretching properties.

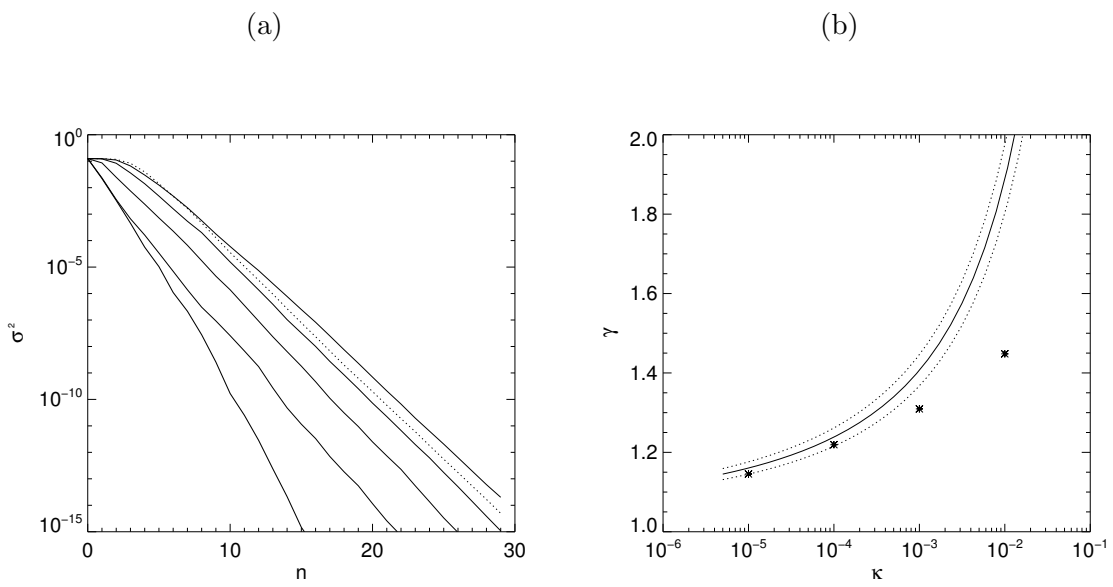

FIG. 2. Variance decay for $P = 1$. (a): variance σ^2 versus n for the forward map with $\kappa = 10^{-5}, 10^{-4}, 10^{-3}, 10^{-2}, 10^{-1}$ (solid lines, from top to bottom), and for the inverse map with $\kappa = 10^{-4}$ (dashed line). (b): decay rate γ versus κ for the forward map. The decay rates, obtained from a least-squares fit over $n \in [5, 30]$ (symbols, with error bars corresponding to the standard error), are compared with the prediction $\bar{\gamma}_{\rm local}$ in (17) (solid line, with dashed lines indicating the error estimates.)

The dependence of γ on κ for the forward map is shown in Fig. 2(b). For each value of κ, γ is obtained from a least-squares fit over the time interval, $n \in [5, 30]$. There is excellent agreement with the asymptotic estimate (17) for $\bar{\gamma}_{\rm local}$. This confirms the applicability of the asymptotic result (9) to the locally controlled regime in more than two dimensions. The agreement deteriorates rather rapidly for larger κ, but this is to be expected since the theory assumes $\kappa \to 0$ and neglects terms that are $o(1/\log^2 \kappa)$.

The spatial structure of the decaying scalar is illustrated by Figs. 3 and 4, which show volume-rendered concentration fields for the forward and inverse maps, respectively. The plots use the normalised concentration variable

$$\theta = \frac{C}{\sigma}, \tag{24}$$

where σ is the the standard deviation defined by (23). This provides a numerical approximation to the strange eigenmode structure $D(\boldsymbol{x}, t)$ defined in (3). To facilitate comparison,

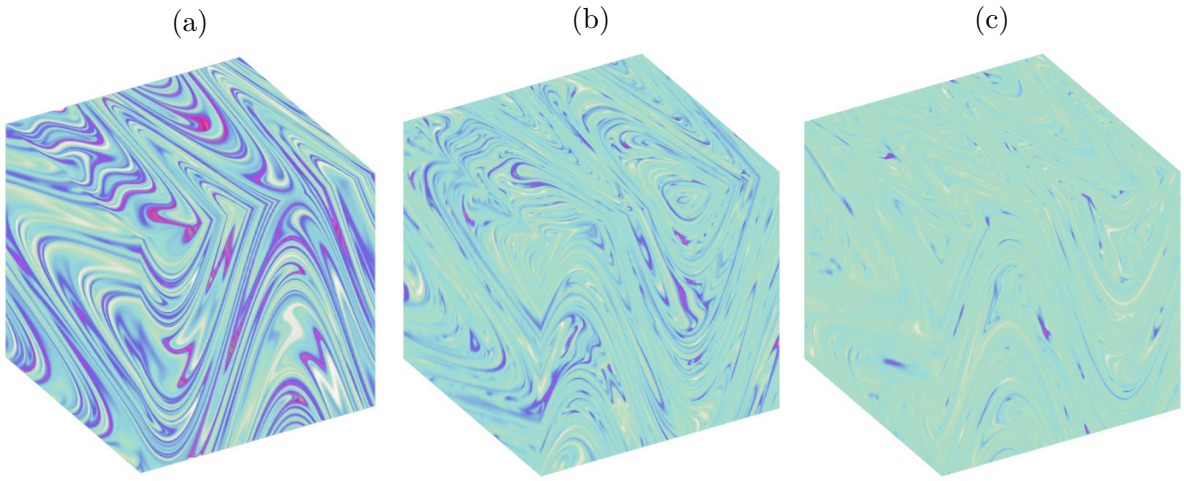

FIG. 3. (Colour online) Concentration field generated by the forward map (14) with $\kappa = 10^{-4}$: (a) $n = 2$; (b) $n = 4$; (c) $n = 6$. Note the presence of filamentary sheets caused by expansion in two directions and contraction in one direction.

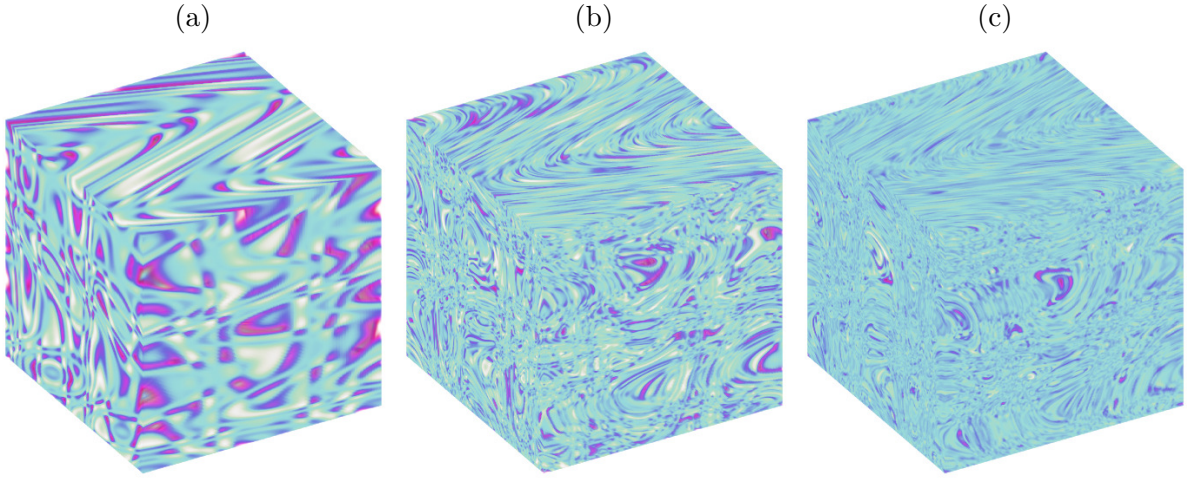

FIG. 4. (Colour online) Concentration field generated by the inverse map (16) with $\kappa = 10^{-4}$: (a) $n = 2$; (b) $n = 4$; (c) $n = 6$. Note the presence of thin "needles" caused by expansion in one direction and contraction in two directions.

the colour scale is renormalised in each panel, i.e., it spans the respective minimum and maximum values.

For the forward map, there is a strong resemblance to the two-dimensional case: large-scale filaments dominate, though in the present case they are manifested as two-dimensional surfaces. This, of course, results from the presence of two expanding and one contracting directions.

For the inverse map, the picture is quite different. In place of the large-scale filamentary sheets, there are now thin "needles", which arise from the presence of two contracting directions. This is most obvious for $n = 4$. Note that these needles are approximately parallel to the (x, y)-plane: the final advection step of each iteration consists of a purely horizontal shear (see (16)) which creates elongated structures in the (x, y)-plane. The contrast between Figs. 3 and 4 underscores the profound effect that differences in the stretching properties of the forward and inverse maps — in particular, the number of positive Lyapunov exponents — have on the structure of the concentration field. It is therefore remarkable that the variance decay rate is insensitive to this. The physical explanation for this result is that the variance for large n is controlled by isolated pockets of extreme concentration values; these pockets, which can be readily identified in Figs. 3c and 4c and correspond to rare events of low stretching [19], have the same statistics in the forward and inverse maps (cf. Sec. II).

V. TRANSITION TO GLOBAL CONTROL: $P > 1$

In this section we examine the transition between the locally controlled and globally controlled regimes by analysing the scalar decay in domains of size $2\pi P$, $P > 1$. We focus on the forward map (14) and fix $\kappa = 10^{-4}$ and $N = 1024$. Simulations have been carried out with the two initial conditions (19) and (20).

A. Variance decay and concentration fields

Fig. 5 summarises the variance decay results by showing the decay rate γ as a function of P. The numerical results are compared with the asymptotic predictions (9) and (10) for the locally and globally controlled regimes. The existence of the two distinct regimes is clear from the figure, with the transition taking place around $P = 3$. The structure of the scalar field for $P = 2$ (see Fig. 6(a)), which is very similar to the structure for $P = 1$, suggests that $P = 2$ is in the locally controlled regime. This is consistent with the argument outlined in Sec. III B which predicts that $P = 3$ corresponds to the smallest domain for global control.

The decay rates found for $P \geq 3$ with the initial conditions (19) are much larger than the approximation to $\bar{\gamma}_{\text{global}}$ provided by homogenisation theory in (10). We attribute this discrepancy to finite-time or symmetry effects: in the homogenisation scenario, the decaying

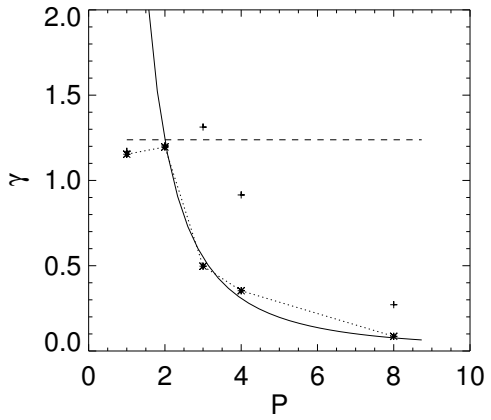

FIG. 5. Decay rate γ versus P for $\kappa = 10^{-4}$. The numerical results obtained with the initial conditions (19) [crosses, $+$] and (20) [asterisks, $*$] are compared with the prediction from homogenisation theory $\bar{\gamma}_{\mathrm{global}}$ (long dashes) and with the prediction $\bar{\gamma}_{\mathrm{local}}$ for the locally controlled regime (solid line).

concentration field has a structure close to that of one of the gravest modes of the diffusion operator, that is $\sin(x/P)$, $\sin(y/P)$ or $\sin(z/P)$, depending on details of the initial conditions. However, in our simulations with the initial conditions (19), the concentration fields are very different (see Figs. 6(b)–(d)). This can be understood as a finite-time effect. As the diffusive approximation of homogenisation theory indicates, the relative amplitudes of the Fourier modes depend on the initial conditions; therefore the high modes can dominate for some finite time if their initial amplitudes are substantially larger than the amplitudes of the gravest modes. This appears to be the case with the initial conditions (19), which would explain why the prediction (10), although valid for $n \gg 1$, is not realised in our simulations (which are limited to $n \leq 30$). Furthermore, for $P \geq 2$ even, the dynamics preserves the symmetries $C(x + P\pi, y, z) = -C(x, y, z)$, $C(x, y + P\pi, z) = -C(x, y, z)$ and $C(x, y, z + P\pi) = -C(x, y, z)$ of the initial conditions (19) (see Figs. 6(a),(c),(d)); however, these symmetries are not compatible with the gravest-mode structure.

To confirm that the discrepancy between simulated and predicted decay rates results from finite-time effects and the special initial conditions, we have repeated the simulations using

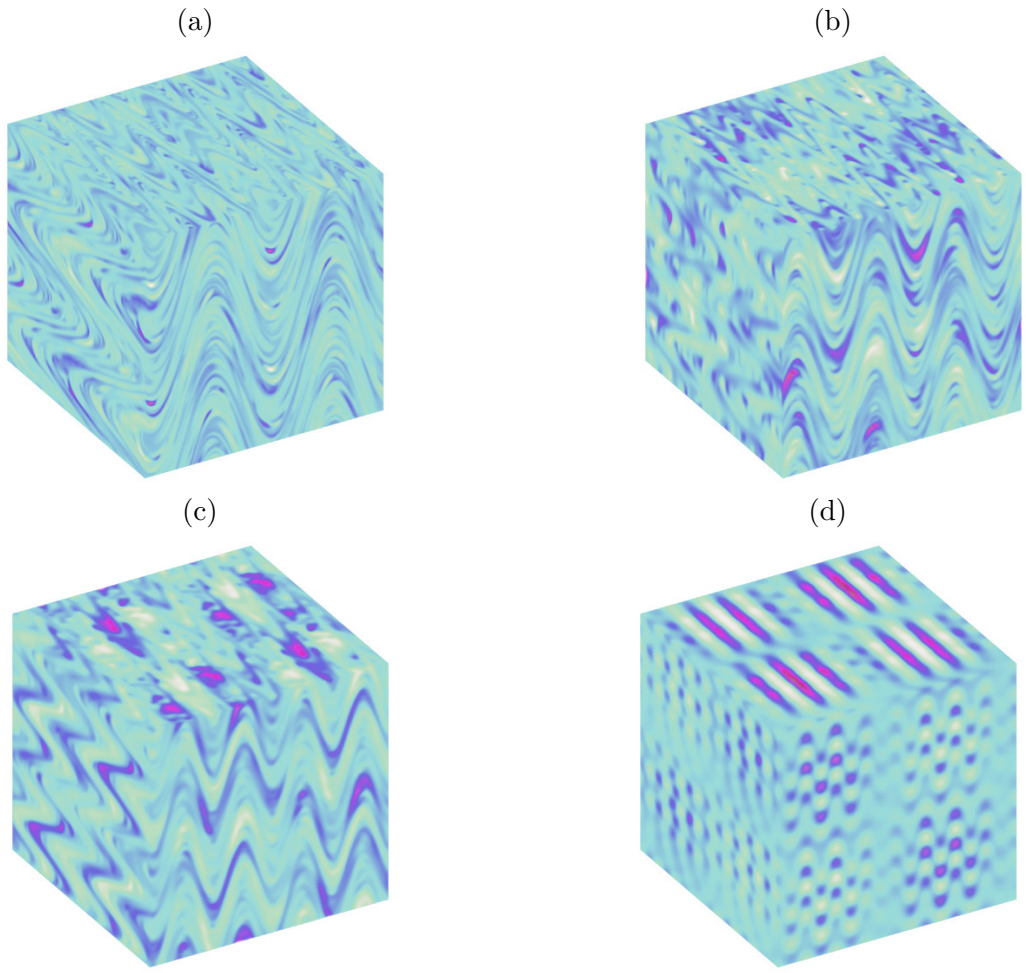

FIG. 6. (Colour online) Concentration fields for $P \geq 2$, $n = 6$ and $\kappa = 10^{-4}$ with initial conditions (19): (a) $P = 2$; (b) $P = 3$; (c) $P = 4$; (d) $P = 8$. Note the transition from a filamentary to a periodic appearance as P is increased.

the gravest mode (20) as initial condition. In this case, the observed decay rates closely match those predicted by homogenisation theory. The scalar fields, displayed in Fig. 7, have the expected structure of a distorted gravest mode for $P \geq 3$, with the distortions reducing as P increases. Comparison between the scalar fields for $P = 2$ and $P = 3$ further supports our claim of local control for $P = 2$.

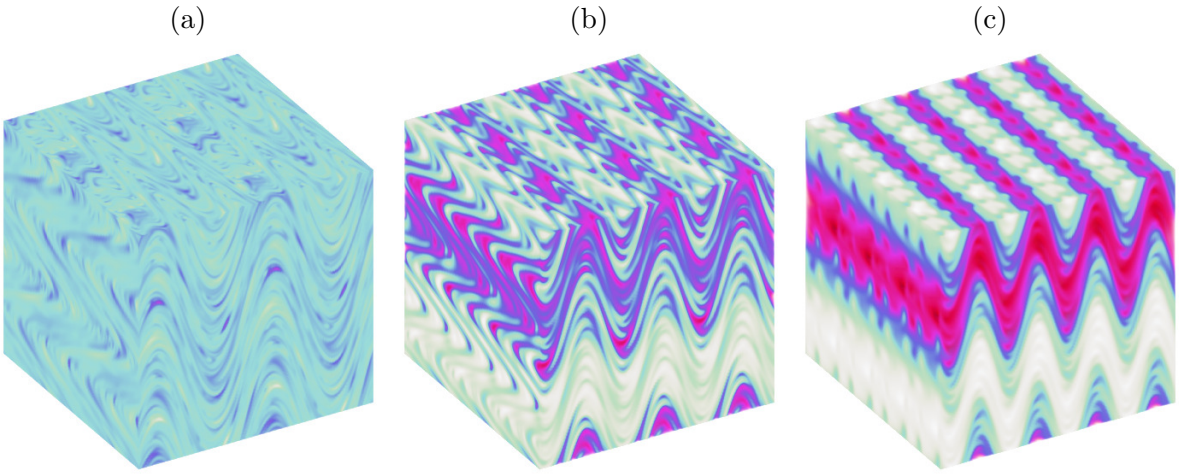

FIG. 7. (Colour online) Concentration fields for $\kappa = 10^{-4}$ with initial conditions (20): (a) $P = 2$; (b) $P = 3$; (b) $P = 4$. As P increases, the structure of the concentration approaches the structure of one of the gravest modes of the diffusion operator, here $\sin z$.

B. Statistical moments and pdfs

An alternative view of the transition from local to global control is provided by statistical moments and pdfs of the concentration field. Normalised moments are defined by

$$m_q = \frac{1}{\sigma}\left(\int C^q dx\right)^{2/q}. \tag{25}$$

According to the strange-eigenmode expression (3), they should be stationary random functions. This was confirmed in numerical simulations of the 2-D sine map, which indicate that the m_q are approximately constant [16]. This is at odds with the predictions of [13] that the m_q depend on q and increase exponentially with time.

Fig. 8 plots m_q against n for various values of P and $q = 4, 6, 8, 10$. Focusing on $P = 1$, the m_q increase rapidly (approximately exponentially) on short timescales before levelling off, in close analogy to the two-dimensional results (see Fig. 3 of [16]). After the initial transient period, the m_q appear roughly independent of n, consistent with (3) and the existence of a statistical equilibrium established by stretching and diffusion. For $P = 2$ the picture is similar, though the initial growth of the m_q is smaller. For $P = 4$ and $P = 8$, by contrast, there is hardly any growth at all. This is consistent with the tracer behaviour being controlled by an effective diffusion for large P.

With regards to the concentration pdfs, Fereday and Haynes [16] argued that the tails

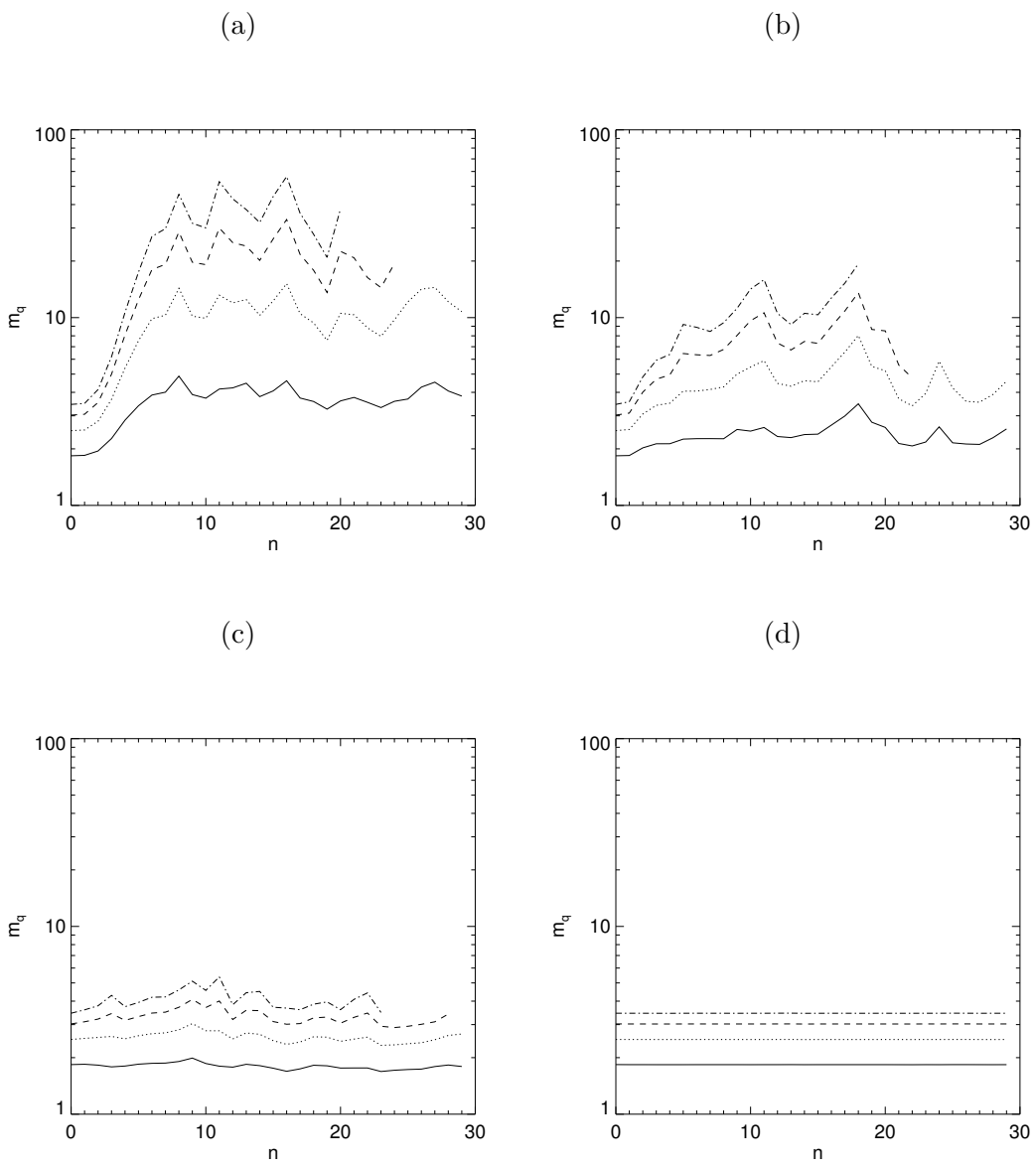

FIG. 8. Time evolution of the moments, m_q vs n, for the forward map with $\kappa = 10^{-4}$: (a) $P = 1$; (b) $P = 2$; (c) $P = 4$; (d) $P = 8$.

should scale like $|\theta|^{-\beta}$ in the limit $\kappa \to 0$, where

$$\beta \sim 1 + 2g(0)/\gamma. \tag{26}$$

This implies that $\beta \sim 3$ in the locally controlled regime, since $\gamma \sim \bar{\gamma}_{\rm local} \sim -\ell(q_*) = g(0)$; on the other hand, $\beta > 3$ in the globally controlled regime, since $\bar{\gamma}_{\rm global} < \bar{\gamma}_{\rm local}$. This prediction was verified in the 2D case [16, 19]. Here we examine this prediction for the forward 3D

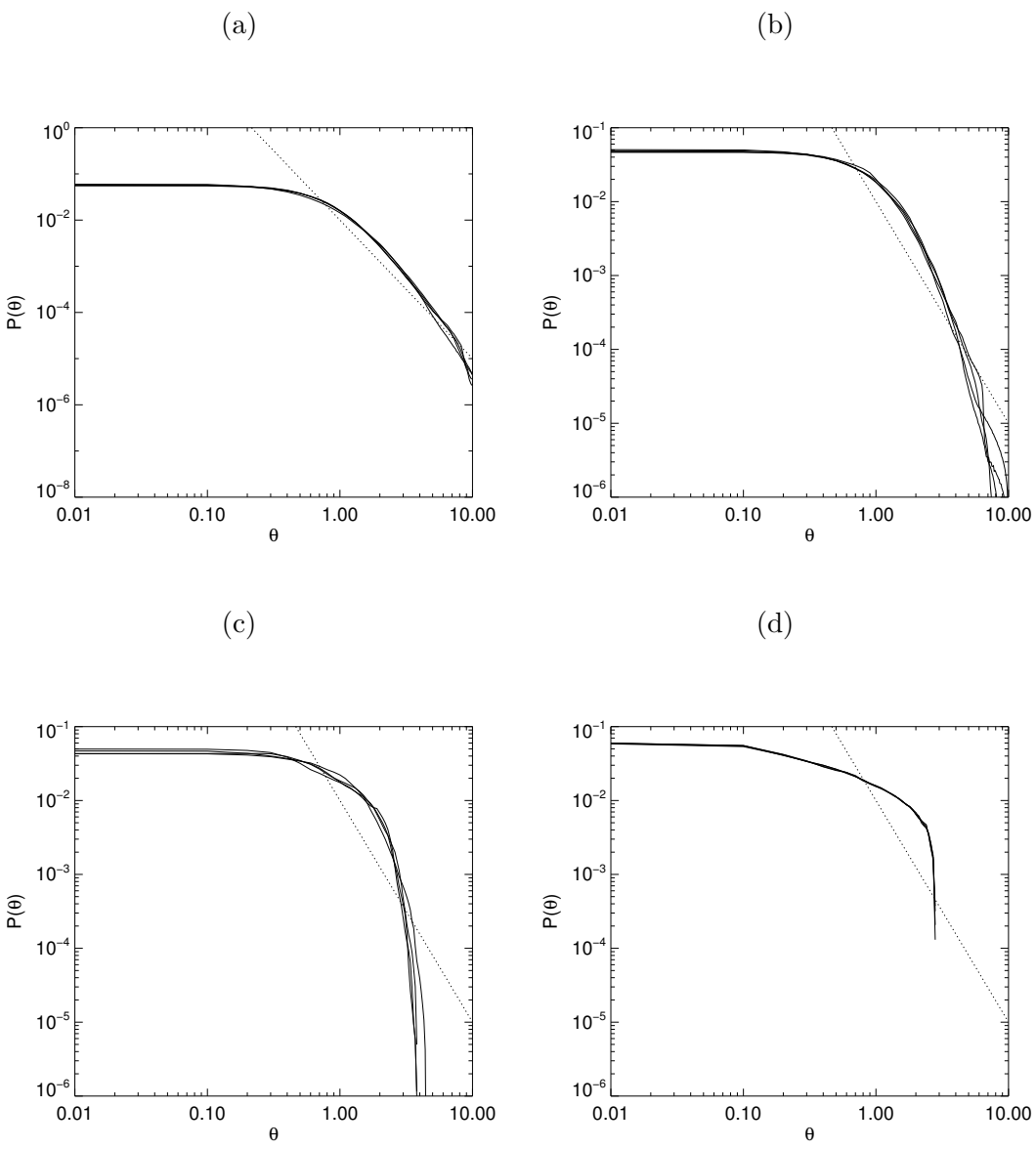

FIG. 9. $p(\theta)$ vs θ for the runs analysed in Fig. 8: (a) $P = 1$; (b) $P = 2$; (c) $P = 4$; (d) $P = 8$. The solid lines correspond to iterations $n = 5, 10, 20, 30$; the reference slope $|\theta^{-3}|$ is plotted with a dotted line. In the global regime (panels c and d), the tails are much shorter. The pdfs are obtained by binning $\theta \in [-10, 10]$ with 200 bins of uniform width.

map (14).

Fig. 9 shows log-log plots of the pdf $p(\theta)$ for the simulations analysed in Fig. 8. The solid lines correspond to pdfs evaluated at $n = 5, 10, 20, 30$, the dotted lines to $|\theta|^{-3}$. We expect the spectral slope of the tails to change as P increases and we move from a local to

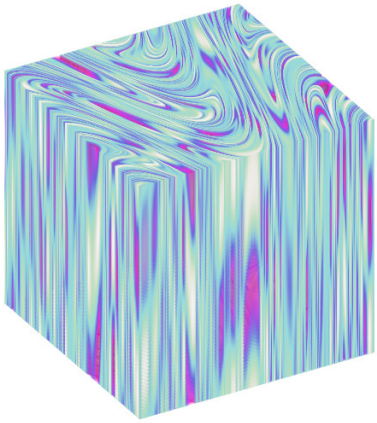

FIG. 10. (Colour online) Concentration field generated by the map (31). $n = 3$ and $\kappa = 10^{-4}$.

global regime. For $P = 1$ the slope is slightly steeper than the theoretical prediction, but the algebraic decay is clear enough. The discrepancy may be related to the finiteness of κ. There is similar behaviour for $P = 2$. For $P = 4$ and $P = 8$, however, the prediction of algebraic tails breaks down. Here the pdfs decays rapidly for $|\theta| > 1$. This is consistent with the concentration field being controlled by an effective diffusion in the homogenisation regime $P \gg 1$.

VI. DISCUSSION

The simulations reported in this paper detail the structure of passive scalars decaying under the combined action of chaotic advection and (molecular) diffusion in 3D. They confirm that the strange-eigenmode behaviour (3), which has been well documented in 2D, carries over to 3D. By contrast with the 2D case, the strange eigenmodes are found to take three different forms, not only depending on whether the decay is locally or globally controlled, but also, in the former case, on the number of positive Lyapunov exponents. Support for this comes from statistical moments, concentration pdfs and fields, and the variance decay.

The simulations confirm that the theoretical predictions of [19] for the decay rate of the concentration variance are valid in 3D as well as in 2D. In particular, the variance decay rate for $\kappa \to 0$ in the locally controlled regime is always given by $g(0) = -\ell(q_*)$ (Fig. 2),

the decay rate of the probability that a line element experience no stretching in the time interval $[0, t]$. As a result, the variance decays at the same rate for the sine map (14) and its inverse (14), despite the very different structures of the scalar fields. The prediction for the variance decay rate in the globally controlled regime (9), which is obtained by applying homogenisation theory and assuming a large ratio of box size to characteristic scales, has also been well verified (Fig. 5). The transition from local to global control occurs when this ratio takes the value $P = 3$, in agreement with an estimate obtained by equating the predictions for the decay rates.

The identical decay rates for the forward and inverse map may seem surprising. However, this can be explained straightforwardly. Physically, the variance decay is controlled by a few small fluid blobs that remain unstretched for long times. The fraction of fluid occupied by these anomalous regions decreases exponentially at a rate that is identical for the forward and inverse maps and unrelated to the number of positive Lyapunov exponents. Mathematically, the equality of the decay rates can be established directly, without resorting to the explicit expression (9) for the decay rate. To see this, let us denote by $\mathcal{T}_n$ the action of a volume-preserving map such as (14) on the concentration field, $C_n = C(\cdot, n\tau)$. Immediately after the nth advection step

$$C_{n+1}(\boldsymbol{x}_{n+1}) = (\mathcal{T}_n C_n)(\boldsymbol{x}_{n+1}) = C_n(\boldsymbol{x}_n) \tag{27}$$

while after the nth diffusion step (i.e. completion of the full nth step)

$$C_{n+1}(\boldsymbol{x}_{n+1}) = (\mathcal{D}\mathcal{T}_n C_n)(\boldsymbol{x}_{n+1}), \tag{28}$$

where $\mathcal{D}$ represents the effect of diffusive smoothing, Using volume preservation, it can be checked that the adjoint (in L_2) of $\mathcal{T}_n$ is $\mathcal{T}_n^\dagger = \mathcal{T}_n^{-1}$ (i.e. $\mathcal{T}_n$ is unitary), while $\mathcal{D}^\dagger = \mathcal{D}$. Now, after $n+1$ steps of the forward map, the concentration field is

$$C_{n+1} = \mathcal{D}\mathcal{T}_n\mathcal{D}\mathcal{T}_{n-1}\cdots\mathcal{D}\mathcal{T}_0 C_0, \tag{29}$$

while after $n+1$ steps of the inverse map it is

$$C_{n+1} = \mathcal{D}\mathcal{T}_n^\dagger\mathcal{D}\mathcal{T}_{n-1}^\dagger\cdots\mathcal{D}\mathcal{T}_1^\dagger C_0. \tag{30}$$

Comparing the operators on the right-hand side of (29) and (30), we see that they are almost adjoints of each another, with differences (relating to the ordering of the $\mathcal{T}_n$ and the position

of $\mathcal{D}$) which are irrelevant to the statistics of C_n as $n \to \infty$ (since the $\mathcal{T}_n$ are iid). Noting that the decay rate λ in (3) can be defined as the largest singular value of these operators, and that operators which are adjoints of each other have the same singular values, we conclude that the decay of the forward and inverse maps are identical.

The prediction (9) for the decay rate in the locally controlled regime applies to flows that are sufficiently mixing. The precise notion of what sufficiently mixing means is not entirely clear, but we expect it to be close to the dynamical-system notion of exponential decay of correlations [35]. One property which plays an important role is that of transitivity of the stretching. This property, which is important for the large-deviation form (5)–(7) of the stretching statistics [36], requires that the tangent map A_n leave no deterministic directions invariant. As noted earlier, not all possible 3D extensions of the 2D sine map satisfy this property. To demonstrate this, we have considered the map

$$x_{n+1} = x_n + a\sin(y_n+\phi_n), \quad y_{n+1} = y_n + b\sin(x_{n+1}+\psi_n), \quad z_{n+1} = z_n + c\sin(y_{n+1}+\varphi_n), \tag{31}$$

as an alternative to (14). The map (31) does not stretch exponentially in the vertical. Consequently the concentration field takes a highly anisotropic form, very different from that obtained for (14): the vertical gradients of concentration are much weaker than the horizontal ones, as illustrated by Fig. 10 which displays the concentration from a scalar-decay simulation using (31) and $\kappa = 10^{-4}$, and the scalar decay is controlled by horizontal stretching. In this case, the decay rate is obtained from (9) by considering the horizontal components of (31) only.

JV acknowledges the support of a Leverhulme Research Fellowship.

---

[1] J. M. Ottino, *The kinematics of mixing : stretching, chaos, and transport* (Cambridge University Press, 1989) p. 364.

[2] G. K. Batchelor, "Small-scale variation of convected quantities like temperature in turbulent fluid. Part 1, General discussion and the case of small convectivity," J. Fluid Mech. **5**, 113–133 (1959).

[3] P. H. Haynes and J. Anglade, "The vertical-scale cascade in atmospheric tracers due to large-scale differential advection," J. Atmos. Sci. **54**, 1121–1136 (1997).

[4] K. Ngan and T. G. Shepherd, "A closer look at chaotic advection in the stratosphere. Part I. Geometric structure," J. Atmos. Sci. **56**, 4134–4152 (1999).

[5] T. Burghelea, E. Segre, and V. Steinberg, "Mixing by polymers: experimental test of decay regime of mixing," Phys. Rev. Lett. **92**, 164501 (2004).

[6] A. Pikovsky and O. Popovych, "Persistent patterns in deterministic mixing flows," Europhys. Lett. **61**, 625–631 (2003).

[7] V. V. Lebedev and K. S. Turitsyn, "Passive scalar evolution in peripheral regions," Phys. Rev. E **69**, 036301 (2004).

[8] H. Salman and P. H. Haynes, "A numerical study of passive scalar evolution in peripheral regions," Phys. Fluids **19**, 067101 (2007).

[9] R. H. Kraichnan, "Small-scale structure of a scalar field convected by turbulence," Phys. Fluids **11**, 945–953 (1968).

[10] R. H. Kraichnan, "Inertial-range transfer in two- and three-dimensional turbulence," J. Fluid Mech. **47**, 525–535 (1971).

[11] G. Falkovich, K. Gawędzki, and M. Vergassola, "Particles and fields in fluid turbulence," Rev. Modern Phys. **73**, 913–975 (2001).

[12] T. M. Antonsen, Z. Fan, E. Ott, and E. Garcia-Lopez, "The role of chaotic orbits in the determination of power spectra of passive scalar," Phys. Fluids **8**, 3094–3104 (1996).

[13] E. Balkovsky and A. Fouxon, "Universal long-time properties of Lagrangian statistics in the Batchelor regime and their application to the passive scalar problem," Phys. Rev. E **60**, 4164–4174 (1999).

[14] D. T. Son, "Turbulent decay of a passive scalar in the Batchelor limit: exact results from a quantum mechanical approach," Phys. Rev. E **59**, R3811 (1999).

[15] D. R. Fereday, P. H. Haynes, A. Wonhas, and J. C. Vassilicos, "Scalar variance decay in chaotic advection and Batchelor-regime turbulence," Phys. Rev. E **65**, 035301 (2002).

[16] D. R. Fereday and P. H. Haynes, "Scalar decay in two-dimensional chaotic advection and Batchelor-regime turbulence," Phys. Fluids **16**, 4359–4370 (2004).

[17] A. A. Schekochihin, P. H. Haynes, and S. C. Cowley, "Diffusion of passive scalar in a finite-scale random flow," Phys. Rev. E. **70**, 046304 (2004).

[18] Y.-K. Tsang, T. M. Antonsen, and E. Ott, "Exponential decay of chaotically advected passive scalars in the zero diffusivity limit," Phys. Rev. E **71**, 066301 (2005).

[19] P. H. Haynes and J. Vanneste, "What controls the decay rate of passive scalars in smooth random flows?." Phys. Fluids **17**, 097103 (2005).

[20] R.S. MacKay, "Transport in 3d volume-preserving flows," J. Nonlin. Sci. **4**, 329–354 (1994).

[21] V. Toussaint, P. Carrière, and F. Raynal, "A numerical approach to mixing by chaotic advection," Phys. Fluids **7**, 2834–2844 (1995).

[22] V. Toussaint, P. Carrière, J. Scott, and J.-N. Gence, "Spectral decay of a passive scalar in chaotic mixing," Phys. Fluids **12**, 2834–2844 (2000).

[23] R. T. Pierrehumbert, "Tracer microstructure in the large-eddy dominated regime," Chaos, Solitons & Fractals **4**, 1091–1110 (1994).

[24] R. T. Pierrehumbert, "Lattice models of advection-diffusion," Chaos **10**, 61–74 (2000).

[25] G. Haller and G. Yuan, "Lagrangian coherent structures and mixing in two-dimensional turbulence," Physica D **147**, 352–370 (2000).

[26] A. Fannjiang, S. Nonnenmacher, and L.Wolowski, "Dissipation time and decay of correlations," Nonlinearity **17**, 1481–1508 (2004).

[27] E. Ott, *Chaos in dynamical systems*, 2nd ed. (Cambridge University Press, 2002) p. 478.

[28] J. Vanneste, "Estimating generalized Lyapunov exponents for products of random matrices," Phys. Rev. E **81**, 036701 (2010).

[29] J. Sukhatme and R. T. Pierrehumbert, "Decay of passive scalars under the action of single scale smooth velocity fields in bounded two-dimensional domains: from non-self-similar probability distribution functions to self-similar eigenmodes," Phys. Rev. E **66**, 056302 (2002).

[30] J.-L. Thiffeault and S. Childress, "Chaotic mixing in a torus map," Chaos **13**, 502–507 (2003).

[31] "Kraichan–Kazantsev flows" are obtained in the limit of zero correlation time for the velocity field (i.e. a white-in-time velocity field); "renewing flows" or "renovating flows" are described by independent, identically distributed random processes that become completely decorrelated after a finite time interval.

[32] A. J. Majda and P. R. Kramer, "Simplified models for turbulent diffusion: theory, numerical modelling and physical phenomena," Phys. Rep. **314**, 237–574 (1999).

[33] J. Vanneste, "Intermittency of passive-scalar decay: strange eigenmodes in random shear flows," Phys. Fluids **18**, 087108 (2006).

[34] Note that [13] predicts a decay rate for $d = 3$ which differs from $\gamma \sim -\ell(q_*) = g(0)$ and depends on whether a flow has one or two expanding directions.

[35] V. Baladi, *Positive transfer operators and decay of correlations*, Vol. 16 (World Scientific, 2000).

[36] P. Bougerol and J. Lacroix, *Products of random matrices with applications to Schrödinger operators* (Birkhäuser, 1985) p. 283pp.